

Bidirectional quantitative scattering microscopy

Kohki Horie¹⁺, Keiichiro Toda²⁺, Takuma Nakamura² and Takuro Ideguchi^{1,2,*}

¹ Department of Physics, The University of Tokyo, Tokyo, Japan

² Institute for Photon Science and Technology, The University of Tokyo, Tokyo, Japan

⁺These authors contributed equally to this work

* Corresponding author: ideguchi@ipst.s.u-tokyo.ac.jp

Abstract

Quantitative phase microscopy (QPM) and interferometric scattering (iSCAT) microscopy are powerful label-free imaging techniques and are widely used for biomedical applications. Each method, however, possesses distinct limitations: QPM, which measures forward scattering (FS), excels at imaging microscale structures but struggles with rapidly moving nanoscale objects, while iSCAT, based on backward scattering (BS), is highly sensitive to nanoscale dynamics but lacks the ability to image microscale structures comprehensively. Here, we introduce bidirectional quantitative scattering microscopy (BiQSM), an innovative approach that integrates FS and BS detection using off-axis digital holography with bidirectional illumination and spatial-frequency multiplexing. BiQSM achieves spatiotemporal consistency and a dynamic range 14 times wider than QPM, enabling simultaneous imaging of nanoscale and microscale cellular components. We demonstrate BiQSM's ability to reveal spatiotemporal behaviors of intracellular structures, with FS-BS correlation analysis providing insights into proteins, lipids, and membranes. Time-lapse imaging of dying cells further highlights BiQSM's potential as a label-free tool for monitoring cellular vital states through structural and motion-related changes. By bridging the strengths of QPM and iSCAT, BiQSM advances quantitative cellular imaging and opens new avenues for studying dynamic biological processes.

Introduction

Quantitative phase microscopy (QPM)^{1,2,3,4,5} provides refractive-index (RI) contrasts of specimens with high spatiotemporal resolution, making it a widely utilized technique for label-free live-cell imaging. Unlike fluorescence microscopy, which offers specific molecular information for a limited number of species, QPM can provide more comprehensive information on cellular images, including dry mass distribution⁶ and the motion behaviors of diverse cellular organelles⁷. QPM visualizes a map of the optical-phase delay (OPD) induced by diffraction from objects by imaging the complex optical field, which consists of forward scattered (FS) and unscattered incident light. In principle, FS contains rich information on microscopic structures ranging from the Rayleigh scattering region (< 100 nm, referred to as “nanoscale” in this study) to the Mie scattering region (> 100 nm, referred to as “microscale” in this study), making QPM well-suited for visualizing complex structures, such as biological cells. However, QPM faces practical challenges in visualizing nanoscale objects within cells due to a limited dynamic range, as these objects move rapidly on the millisecond timescale. Consequently, QPM has been primarily employed for imaging static or slowly changing microscale structures.

On the contrary, backward scattering (BS) detection is recognized for enabling the measurement of rapidly moving nanoscale objects, as BS predominantly contains Rayleigh scattering. Interferometric scattering (iSCAT) microscopy^{8,9} is a notable BS-based imaging method that has demonstrated high sensitivity for in vitro imaging of nanoscale objects, such as 2-nm gold nanoparticles (GNPs)¹⁰ and single proteins¹¹. Recently, iSCAT has been applied to in vivo imaging of intracellular vesicles¹² and viruses¹³, as well as characterizing molecular diffusion dynamics through particle tracking¹² and time-domain frequency analysis¹⁴. However, BS detection inherently lacks sensitivity to microscale structures due to the limited detectability in the Mie scattering region, resulting in iSCAT’s inability to deliver comprehensive quantitative cellular imaging, a capability that QPM offers.

In this work, we address the aforementioned trade-off by integrating the concepts of QPM and iSCAT within a new framework of bidirectional quantitative scattering microscopy (BiQSM), where quantitative complex field images of FS and BS are simultaneously captured. Our BiQSM is based on off-axis digital holography (DH) with bidirectional illumination and the spatial-frequency multiplexing method¹⁵ for capturing both FS and BS images simultaneously. This optical configuration enables the use of a single objective lens and an image sensor, ensuring spatiotemporal consistency between the FS and BS complex-field images. Our BiQSM achieves an exceptionally wide dynamic range in scattering imaging, an order of magnitude wider than that of QPM, allowing for the simultaneous visualization of both rapidly moving nanoscale particles and slowly moving microscale structures. Moreover, the concurrent imaging of FS and BS allows for correlation analysis within the microscale Mie scattering region, with each modality capturing distinct and complementary information.

We initially present a 14-fold enhancement in the dynamic range of BiQSM compared to QPM. Furthermore, we underscore the significance of correlation analysis between FS and BS data by imaging nanoparticles in the Mie scattering region, which remain indistinguishable when analyzed using FS alone. Subsequently, we present wide dynamic range live-cell imaging, enabling simultaneous visualization of both the spatial distribution and dynamic

behavior of microscale intracellular structures (e.g., lipid droplets) and nanoscale structures via FS and BS imaging, respectively. Correlation analysis between FS and BS images allows characterization of the moving entities observed in BS, which include principal dry mass constituents such as proteins and lipids, as well as components independent of dry mass quantity, like the cell membrane. Finally, through time-lapse live-cell observation during the cellular dying process, we exhibit the potential of BiQSM as a powerful label-free tool for monitoring cellular vital states through the acquisition of significant spatiotemporal modifications.

Results

Principle of BiQSM.

The schematic representation of Rayleigh and Mie scattering is illustrated in Fig. 1a. In Rayleigh scattering, which arises from nanoscale objects, both FS and BS waves exhibit constructive interference owing to negligible optical path length differences of the scattered light, resulting in identical FS and BS intensities. Note that nanoscale objects also include thin structures along the axial direction, such as cell membranes, although these structures possess microscale features in the lateral dimension. In contrast, Mie scattering, which arises from microscale objects, involves constructive interference of FS waves from any depth within the sample, whereas BS waves may undergo destructive interference due to varying path lengths from different depths. This results in a pronounced intensity disparity between FS and BS (see Fig. 1a bottom). In particular, the BS intensity is saturated for objects larger than $\sim 1 \mu\text{m}$ (near the wavelength of illumination light), leading to information loss of microscale objects.

We define the amplitude ratios between the scattered wave E_s and the incident illumination wave E_i , hereafter referred to as scattering-field amplitude (SA), as a parameter to characterize the bidirectionally scattering fields within a unified framework, facilitating direct comparison between FS and BS images. Figure 1b illustrates the phasor diagrams of the FS and BS fields, where E_{sample} and E_{bg} represent the measured fields with and without a sample, respectively, following the relation $E_{\text{sample}} = E_{\text{bg}} + E_s$. Using the measured complex amplitude of the E_{sample} , we can derive the SA as:

$$SA = \frac{|E_s|}{|E_i|} = \frac{|E_{\text{sample}} - E_{\text{bg}}|}{|E_{\text{bg}}/\alpha|} = \alpha \frac{|E_{\text{sample}} - E_{\text{bg}}|}{|E_{\text{bg}}|}, \quad (\text{Eq. 1})$$

where α is a constant value defined as $E_{\text{bg}} = \alpha E_i$, which is field transmittance and reflectivity of the glass sample holder. The α value is 1 and 0.07 for FS and BS imaging, respectively, representing that fully transmitted light goes into the image sensor in FS imaging, while partially reflected light from the coverslip-water interface reaches the image sensor in BS imaging. The SA value ranges between 0 and 2 by definition.

Figure 1c illustrates the dynamic ranges of single-frame SA for QPM (FS measurement), iSCAT (BS measurement), and BiQSM (simultaneous FS and BS measurement), all operating under optical shot noise limitations. This figure shows an order-of-magnitude sensitivity enhancement of BS measurement, which is pivotal for the dynamic-range

expansion of our BiQSM. Figure 1d represents illustrative schematics of FS and BS imaging, along with the photon budget of the image sensor. In FS imaging, the dominant components are the unscattered, transmitted light ($|E_{bg}|^2 = |E_i|^2$) and the strong Mie scattered light from microscale cellular structures, resulting in a small portion of Rayleigh scattered light from nanoscale objects. In contrast, in BS imaging, fewer photons from the substrate reflection ($|E_{bg}|^2 = 0.07^2 |E_i|^2$) reach the image sensor due to the epi-illumination configuration. Therefore, the contribution of Rayleigh-scattered light to the photon budget increases by a factor of 14 ($1/0.07$) by 204-times stronger illumination without saturating the image sensor. Additionally, BS offers higher sensitivity for Rayleigh scattering because BS from microscale structures is weaker than FS.

BiQSM enables bidirectional scattering imaging with spatiotemporal consistency by simultaneously capturing FS and BS images using a single detection system. This capability is critical for correlative analysis between FS and BS microscopic images, particularly for samples with densely packed, dynamically varying fine structures, such as cells, where numerical compensation for spatial inconsistencies between different microscopy systems poses significant challenges. To achieve this, bidirectional illumination is applied to the sample from opposite directions, and FS and BS light are simultaneously detected using a single image sensor. The spatial-frequency multiplexing method of off-axis DH¹⁵ is employed to capture both images simultaneously (see Fig. 1d, “BiQSM system” in Methods, and Supplementary Note 1 for details). This method encodes FS and BS information into separate frequency domains by employing distinct off-axis angles for the reference light, enabling selective reconstruction of FS and BS images from a single hologram (see Fig. 1e).

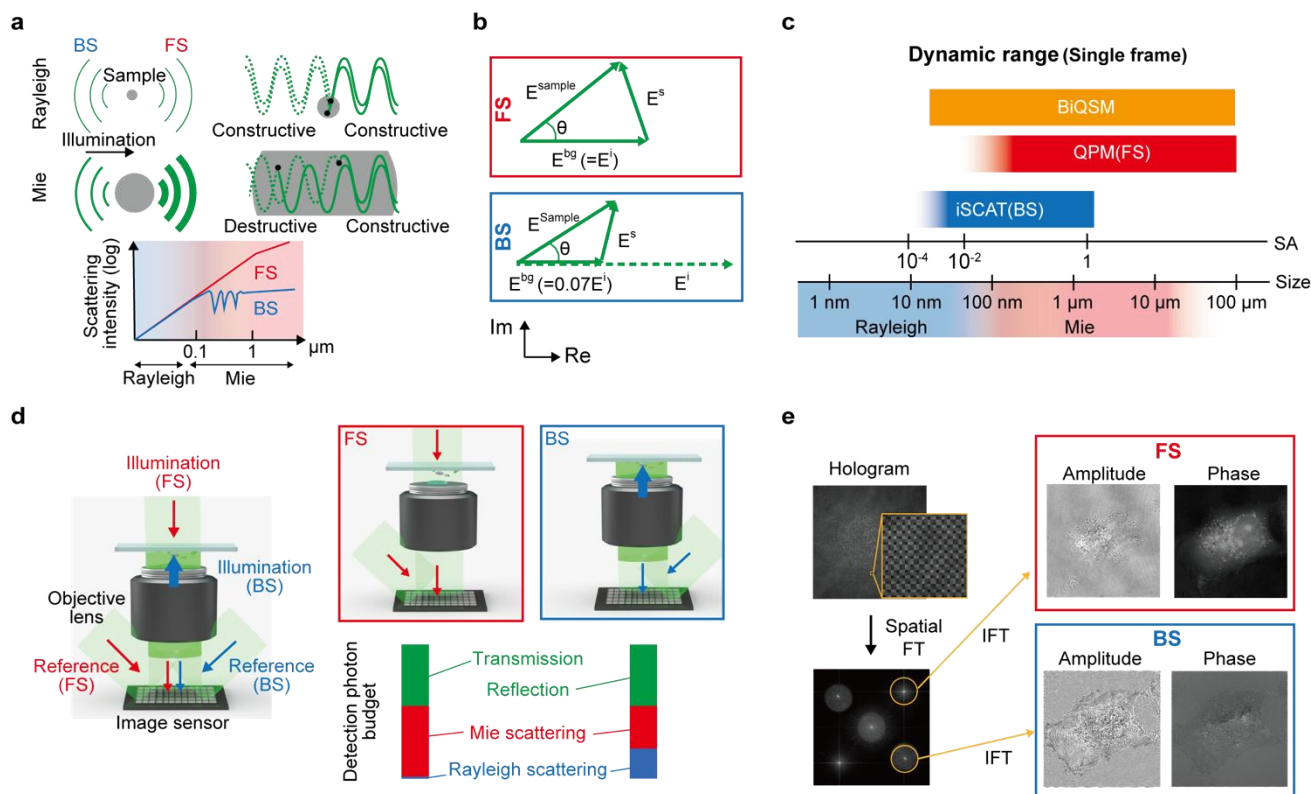


Figure 1 Principle and schematic of the BiQSM system. a Physical representation of Mie and Rayleigh scattering.

b Phasor diagrams of the FS and BS fields, illustrating the relationship among E_i , E_s , and the measured fields with and without a sample (E_{sample} and E_{bg}). **c** Single-shot SA dynamic range of BiQSM, QPM (FS), and iSCAT (BS), along with the typical size of scattering objects within biological cells. Note that we assume a QPM technique based on interferometry, such as off-axis DH, to calculate the SA dynamic range. **d** Illustrative schematics of FS and BS imaging, along with the photon budget of the image sensor. **e** Reconstruction process of FS and BS images from a single hologram.

Demonstration of dynamic range expansion and correlation analysis between FS and BS images.

To demonstrate the dynamic range expansion with our BiQSM, we evaluated the single-frame minimum detectable SAs for FS and BS imaging by measuring their temporal standard deviations in the absence of samples (see “Temporal noise calculation” in Methods). The evaluated minimum detectable SAs were 6.5×10^{-3} and 4.6×10^{-4} for FS and BS, respectively, highlighting the superior sensitivity of BS imaging by a factor of 14. These values are consistent with those predicted by optical shot noise, corresponding to scattering signals from 90-nm and 30-nm silica beads ($n=1.43$) in an aqueous environment.

Then, we measured a 50-nm silica bead to validate this evaluation. Figure 2a presents the FS- and BS-SA images, reconstructed from the measured complex amplitude images using Eq. 1. We imaged a flowing bead to obtain E_{sample} and E_{bg} images from consecutive frames within the same FOV, effectively eliminating temporally static background noise caused by the surface roughness of the glass substrate. In this study, we refer to this approach as temporal differential analysis. As expected from the evaluated minimum detectable SAs, the 50-nm silica bead was detected solely through BS imaging.

Next, we verified the advantage of correlation analysis between FS and BS images using the SA images of a 150-nm polystyrene bead and a 200-nm silica bead, as shown in Fig. 2b (see “Preparation of samples” in Methods for details of the sample). Figure 2c displays the scattering cross-sections of the beads for FS and BS images, derived by spatially integrating the squares of the SA images. The data are normalized by the average cross-section values of the polystyrene beads (see “Beads measurement” in Methods for the calculation procedure). The results show that while the FS cross-sections of the two beads overlap, their BS cross-sections differ, demonstrating that FS-BS correlation analysis effectively differentiates these beads. Note that other sets of beads may exhibit overlapping BS cross-sections but not FS cross-sections, depending on their refractive index (RI) and size combination. FS-BS correlation analysis also provides the ability to decouple RI and size from the SAs, enabling precise determination of bead properties. For instance, the RI and size of the silica beads were evaluated as 1.426 ± 0.006 and 206 ± 18 nm, respectively, closely aligning with the manufacturer’s specifications of 1.43 and 203 ± 12 nm (see Supplementary Note 2 for details). The precision of this particle characterization is not limited by the optical shot noise but is likely influenced by two factors: size variation in the beads and systematic error in the numerical focusing process, as discussed in Supplementary Note 2. This capability of quantitative particle characterization holds significant potential for studying bioparticles, as further explored in the Discussion section.

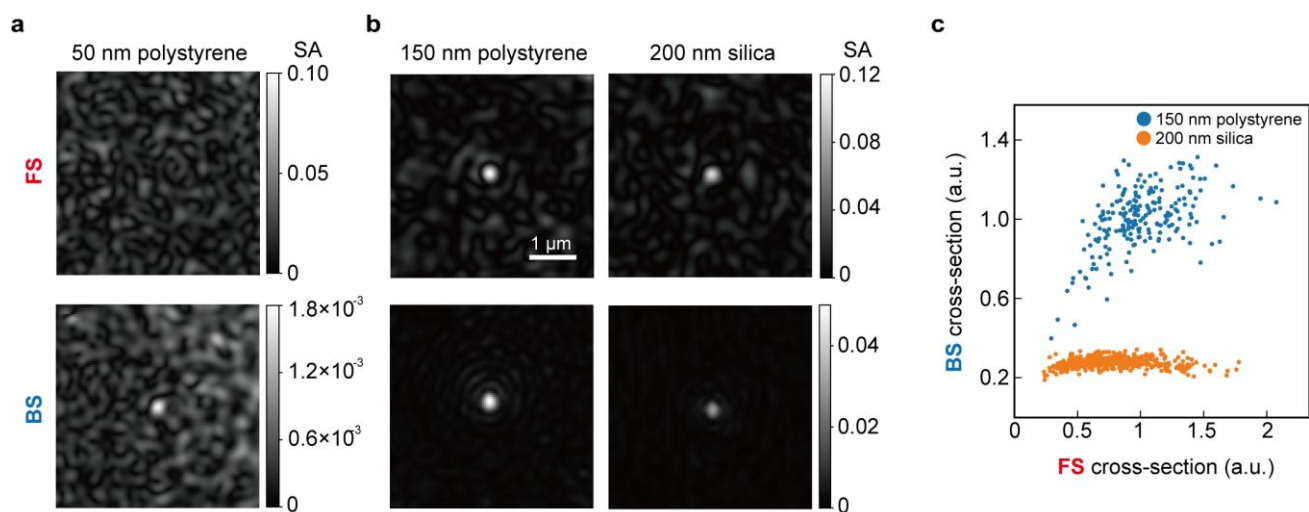


Figure 2 Dynamic range expansion and FS-BS correlation analysis through bidirectional scattering imaging of nanometer-scale beads. SA images of **a** a 50-nm silica bead, and **b** a 150-nm polystyrene bead, and a 200-nm silica bead. **c** Scattering cross-sections of 150-nm polystyrene beads (151 ± 3 nm, 204 particles) and 200-nm silica beads (203 ± 12 nm, 412 particles) normalized by average values of 150-nm polystyrene beads.

Bidirectional quantitative scattering imaging of living cells.

We applied BiQSM to live-cell imaging. Figure 3a displays FS- and BS-SA images of COS7 cells (hereafter referred to as “static images”). The static FS image reveals the global structure of a cell and microscale cellular organelles, including the nucleus, nucleoli, and lipid droplets, with SA values up to ~ 2 . The global SA distribution within the cell reflects the spatial distribution of depth-integrated dry mass concentration, which is crucial for monitoring cellular states or growth rates⁶. We validated that the microscale particles detected in FS imaging (e.g., particles indicated by white arrows) are predominantly lipid droplets by molecular bond-specific imaging techniques¹⁶. In contrast, the static BS image reveals nanoscale structures with SA values an order of magnitude smaller. For instance, as shown in the inset of Fig. 3b, Newton’s ring-like interference patterns were observed with an SA of less than 0.01. This interference originates from the reflections on the cell membranes, enabling the evaluation of the cellular height map.

To visualize nanoscale particles, we employed temporal differential analysis of consecutive frames, as used in Fig. 2. Figure 3c represents zoomed FS and BS temporal differential images, revealing that a nanoscale particle, comparable to or smaller than the spatial resolution, was detected exclusively in the BS image. The observed SA value of ~ 0.04 suggests that it is likely a small lipid droplet with an RI of ~ 1.45 rather than intracellular vesicles with a lower refractive index (~ 1.37)¹⁷. Detecting such small lipid droplets is crucial for investigating the dynamics of lipid metabolism¹⁸. The background signal in the FS image is not caused by instrumental noise but by motion fluctuations of microscale cellular structures, making it difficult to visualize small particles. In contrast, BS imaging is less sensitive to microscale structures, enabling highly sensitive detection of nanoscale particles with reduced background

signals.

Although the static and temporal differential SA images have already demonstrated the advantages of this microscope, dynamic image analyses provide even greater insights, particularly for analyzing living cells with rapidly moving particles within slowly drifting larger structures. To visualize these dynamic variations, we continuously captured SA images at 500 fps over 10 seconds, generating a time-series dataset of 5,000 frames. We then conducted time-domain frequency analysis¹⁹ to map the temporal SA fluctuations of each pixel within two specific frequency bands: 1-10 Hz (hereafter referred to as low frequency, LF) and 100-250 Hz (high frequency, HF). The LF range was selected to maximize contrast from microscale structures while minimizing the influence of slowly varying background noise caused by air fluctuations and sample stage drift. This range also corresponds to the timescale of characteristic intracellular biomolecular movements driven by bioactivity, distinct from Brownian motion²⁰. The HF range was chosen to enhance contrast relative to the LF image. Similar to temporal differential analysis, this approach also visualizes smaller SA values than background static noise caused by the surface roughness of the glass substrate, thereby fully leveraging the wide dynamic range capability of BiQSM.

Figures 3d and 3e show dynamic LF and HF images for both FS and BS imaging. The signal intensity reflects the object's SA and the strength of its movement within the specified frequency ranges, while the spatial broadening of the signal indicates the object's traveling area. We first discuss the FS images. The dynamic LF- and HF-FS images reveal the motion of large lipid droplets, which are also identified in the static FS image. In the dynamic images, droplets indicated by white arrows exhibit spatially broadened signals compared to those indicated by blue arrows, whereas these signals are indistinguishable in the static image. Moreover, the HF-FS signals for these droplets are significantly weaker than the LF-FS signals. These observations suggest that the microscale droplets (white arrows) undergo slower, longer-range movement compared to those in the surrounding region (blue arrows), highlighting the heterogeneity of intracellular fluidity.

Next, we discuss the BS images. The dynamic LF- and HF-BS images show evident signals in the nucleus, whereas both FS images display signal intensities comparable to the noise level observed outside the cell. The nucleus images reveal a distinct spatial pattern, which may reflect nuclear membrane fluctuations and/or chromatin dynamics. Furthermore, the dynamic HF-BS image highlights localized high-contrast signals (indicated by green arrows) that are undetectable in the LF-BS image, potentially attributed to rapidly fluctuating nanoscale structures. These observations suggest that the dynamic BS images provide unique information not captured by their FS counterparts, likely owing to the dynamic motion of nanoscale objects.

To further characterize the dynamic BS signals, we performed FS-BS correlation analysis. Figure 3f displays a comparative plot of pixel intensities between the dynamic HF-BS and their corresponding static FS images within the cytoplasm (the red square in Fig. 3a), particularly where distinct microscale structures are absent. Note that the static FS signal intensity is proportional to intracellular dry mass. The plot reveals a linear relation (shown with the green dashed line) with an offset (indicated by the gray arrow), suggesting the existence of two distinct components.

The linear relationship can originate from the dynamic movement of the primary dry mass constituents, such as proteins and lipids, whereas the offset suggests a signal source independent of dry mass quantity, such as the cell membrane. Similar characteristics were observed in the correlation between the dynamic LF-BS and static FS signals.

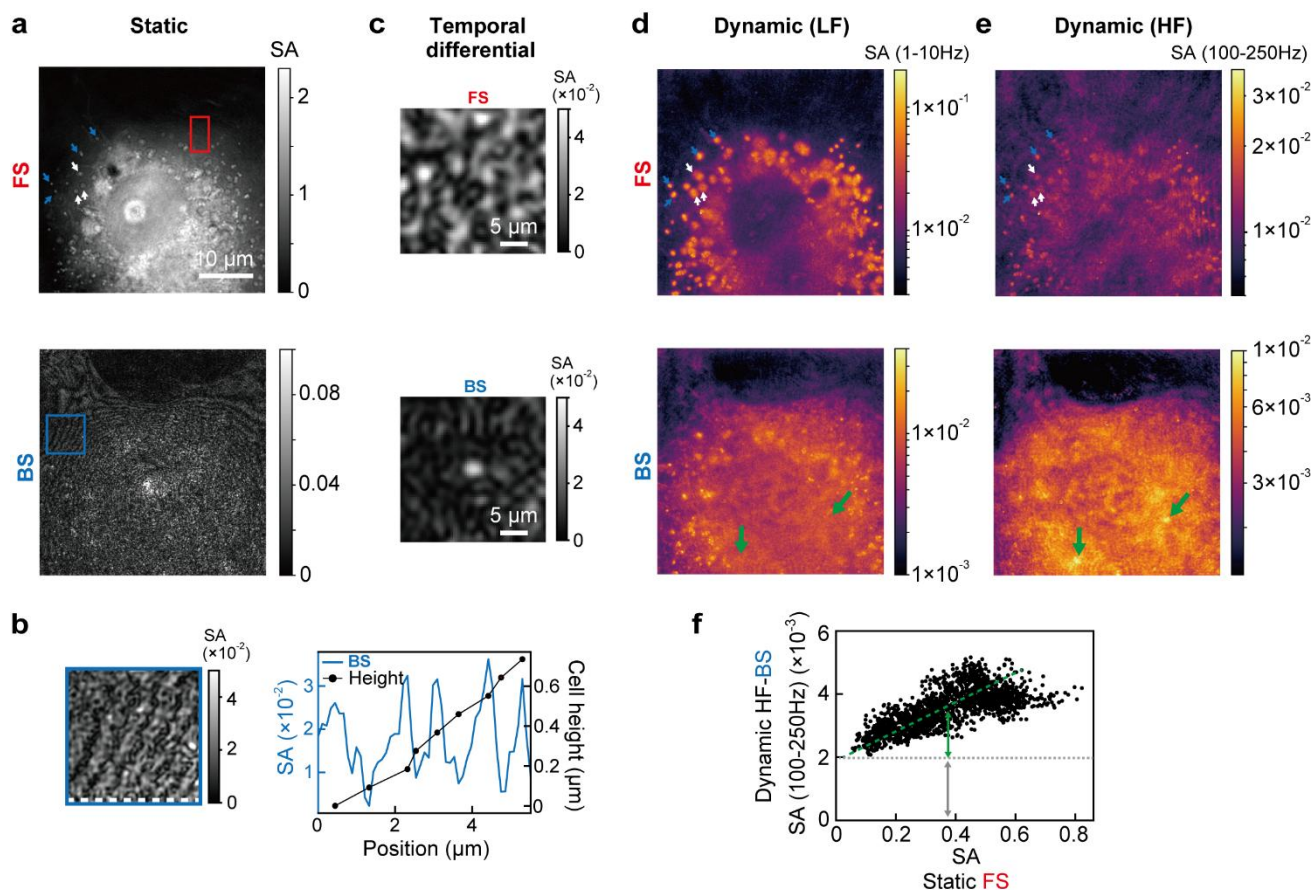


Figure 3 Live-cell imaging with BiQSM. **a** Static FS (top) and BS (bottom) images. **b** Left: Zoomed-in image within the blue square regions in **a**, Right: Cross-sectional profile along the white dashed line in the left image with estimated cell height. **c** FS and BS images of an intracellular small particle visualized with temporal differential analysis of consecutive frames. **d** Dynamic LF-FS (top) and LF-BS (bottom) images. **e** Dynamic HF-FS (top) and HF-BS (bottom) images. **f** Relationship between static FS and dynamic HF-BS signals in the cytoplasm within the red squared region in **a**.

Time-lapse observation of intracellular structures and their dynamic motions in the cellular dying process.

To demonstrate the unique capability of dynamic motion measurement with BiQSM, we conducted a time-lapse observation of the cellular dying process, during which various phenomena, including cell contraction, bleb formation, and ATP depletion, could be observed²¹. Figure 4a presents static FS, dynamic LF-FS, and dynamic LF- and HF-BS images captured at 0, 26, and 53 minutes after the beginning of the measurement under ambient conditions at room temperature, without CO₂ regulation. The static FS image at 53 minutes reveals microscale structural changes, such as alterations in nuclear shape and bleb formation (indicated by white arrows), suggesting the occurrence of cellular

death. Figure 4b illustrates the temporal variations in dynamic SA signals within characteristic regions. A microscale particle-rich region within the cytoplasm exhibits distinct features in dynamic FS images, while particle-less cytoplasmic and nuclear regions present characteristic features in dynamic BS images. The LF-FS image and its temporal evolution reveal that the motion of microscale particles, such as lipid droplets, is transiently activated between 10 and 26 minutes (highlighted in green in Fig. 4b, hereinafter referred to as “Stage 1”), and subsequently damped between 26 and 53 minutes (highlighted in pink in Fig. 4b, hereinafter referred to as “Stage 2”). The transient activation and damping behaviors may be related to changes in intracellular ATP concentration^{20,22}.

BS signals also exhibit characteristic behaviors. LF-BS signals, representing slow fluctuations of nanoscale objects, dropped to ~50% in particle-less and nuclear regions during Stage 2, whereas HF-BS signals, which reflect fast fluctuations of nanoscale objects, increased by ~50% during Stage 1. To further explore these distinct temporal evolutions of LF- and HF-BS signals, we conducted correlation analyses between static FS and dynamic BS images within the particle-less region in the cytoplasm. Figure 4c shows the changes in characteristics at $t = 0$ and 53 minutes. The correlation between LF-BS against static FS reveals a decline in the slope of the linear relationship, indicating reduced movement of primary dry mass constituents (e.g., macromolecules, such as proteins and lipids), while the offset remains unchanged. These observations suggest that the dominant factor contributing to signal decay during Stage 2 is the reduction in motion of macromolecules such as proteins and lipids. In contrast, the correlation between HF-BS against static FS shows an increased offset over time, implying enhanced motion of components independent of dry mass quantity (e.g., the cell membrane), while the linear slope remains unchanged. Consequently, the substantial signal increase observed during Stage 1 may be driven by increased fluctuations in the cell membrane.

It is worth mentioning that intriguing inter-spatial synchronizations between BS and FS signals occur across different locations. The decrease in the LF-BS signal in particle-less and nuclear regions during Stage 2 synchronizes with the LF-FS signal in the microscale particle-rich region. In contrast, the increase in the HF-BS signal during Stage 1 coincides with the activation of microscale particle movement observed in the LF-FS signal at the microscale particle-rich region. These findings suggest that intracellular components of various sizes may undergo distinct yet interconnected phenomena during the process of cellular death.

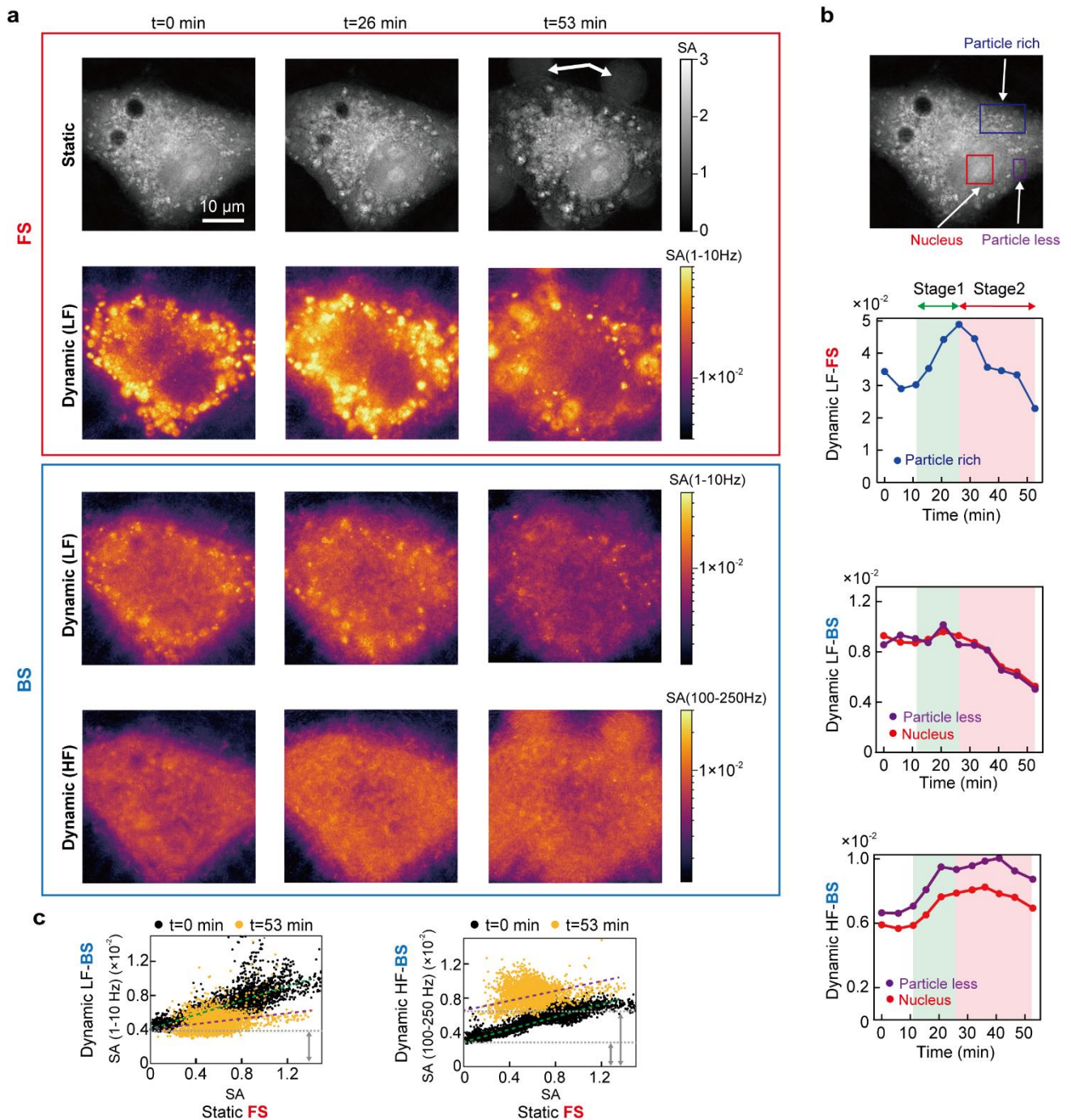


Figure 4 Time-lapse observation of intracellular structures and their dynamic motions in the process of cell death. **a** Static FS, Dynamic LF-FS, Dynamic LF-BS, and Dynamic HF-BS images at 0, 26, and 53 min, respectively. **b** Temporal evolution of dynamic signals within the characteristic regions: A microscale particle-rich region within the cytoplasm for dynamic FS images (blue), and less-particle cytoplasmic and nuclear regions (purple and red) for dynamic BS images. **c** Relationship between static FS signals, and dynamic LF- or HF-BS signals within the cytoplasm at 0 and 53 min.

Discussion

We discuss the advantages of BiQSM over other state-of-the-art microscopy techniques that aim for sensitivity enhancement, particularly dark-field (DF) microscopy²³, coherent bright-field (COBRI) microscopy²⁴, and adaptive dynamic range shift (ADRIFT)-QPM²⁵. In DF and COBRI microscopy, a spatial filter is introduced in the Fourier plane to cut or attenuate both the unscattered light and the strong Mie-scattered light from microscale structures. While this approach enhances sensitivity to Rayleigh scattering from nanoscale objects, similar to iSCAT, it inevitably leads to the loss of microscale structural information, even in FS measurements. Consequently, these techniques are not well-suited for achieving wide-dynamic-range cellular imaging. In contrast, the ADRIFT approach effectively mitigates this limitation by employing wavefront shaping techniques. However, BiQSM has two notable advantages over ADRIFT-QPM. Firstly, while ADRIFT-QPM enhances the sensitivity of FS imaging, its ability to detect small particles in living cells is constrained by microscale structural dynamics. In contrast, BiQSM integrates BS imaging, enabling the visualization of nanoscale particles within living cells with higher precision. Secondly, BiQSM facilitates FS-BS correlation analysis, providing a more comprehensive assessment of scattering phenomena.

Recently, another study demonstrated a dual-modal FS and BS imaging technique in the DF configuration, employing two image sensors with distinct illumination wavelengths²⁶. This system was specifically designed for *in vitro* single-nanoparticle sizing, rather than wide-dynamic-range live-cell imaging. In this approach, the DF configuration shifts the FS dynamic range toward the low-scattering nanoscale region, enabling FS-BS correlation analysis for smaller particles with diameters below 340 nm. However, this shift inherently restricts the ability to visualize microscale intracellular structures. In contrast, BiQSM expands the dynamic range for live cell imaging by integrating FS and BS imaging without shifting the FS dynamic range. Additionally, BiQSM acquires both FS and BS signals using a single image sensor, ensuring high spatial consistency in correlation analysis—an essential attribute for studying dense samples, such as cells.

There is room for technical improvement of BiQSM. Firstly, the dynamic range of BiQSM, currently constrained by optical shot noise, could be further extended by increasing the number of detected photons. For instance, implementing a CMOS sensor with a higher full-well capacity (e.g., the Q-2HFW, Adimec) can improve sensitivity by a factor of ~ 6 . Secondly, the bidirectional approach can be adapted to high-dynamic-range optical diffraction tomography (ODT). In addition to expanding dynamic range, dual-modal acquisition of FS and BS images also improves axial spatial resolution²⁷, as BS information compensates for missing spatial-frequency components along the axial direction in FS imaging. Thirdly, chemical contrast can be integrated into BiQSM by combining it with label-free molecular vibrational imaging modalities, such as mid-infrared²⁸ and Raman microscopy²⁹. In particular, integration with mid-infrared photothermal microscopy¹⁶ could be seamlessly accomplished by incorporating mid-infrared illumination into the BiQSM system. Finally, acquiring additional molecular specific information through fluorescence microscopy could provide valuable insights into the unidentified contrasts observed in this study.

Finally, we discuss future perspectives based on the findings of this study. The quantitative analysis of size and refractive index using FS and BS information (as demonstrated with beads in Fig. 2) can be extended to characterize

various small biological particles with sizes from 100 nm to 1 μm , such as exosomes, both inside and outside cells. This would provide valuable insights into intercellular communication³⁰. Although the current BiQSM system, operating under shot-noise-limited conditions, can detect extracellular particles as small as ~ 100 nm in both FS and BS imaging, intracellular particles smaller than 300 nm remain undetectable in FS imaging due to substantial background signals, as illustrated in Fig. 3c. These background signals likely originate from the dynamic motion of microscale structures spanning multiple depth layers. To address this limitation, adopting a depth-resolved approach, such as three-dimensional BiQSM, could selectively suppress background signals from irrelevant depth layers, thereby enhancing the detectability of target particles.

In another direction, we can further investigate the dynamics presented in Fig. 4. During Stage 2, we observed a synchronized attenuation in the movements of microscale particles (lipid droplets) and nanoscale molecules (proteins, lipids), both of which are diffusible cellular contents. A previous study³¹ hypothesized that intracellular fluidity, modulated by ATP-driven fluctuations in actin filaments, accelerates the movement of diffusible cellular components. This suggests that the attenuation observed in Stage 2 may indicate a reduction in intracellular fluidity due to ATP depletion. A comprehensive temporal analysis using fluorescence-integrated BiQSM would enable detailed investigations of actin filament dynamics and ATP distribution, providing novel insights into the intricate dynamics of the living cellular environment. Additionally, the activation of microscale particle motion (lipid droplets) and dry mass-independent components (potentially the cellular membrane) observed during Stage 1 could also be explored further through fluorescence imaging. Once these underlying mechanisms are better understood, such attenuation or activation events could potentially serve as a diagnostic tool for the early detection of cellular death.

References

1. Park, Y. K. *et al.* Quantitative phase imaging in biomedicine. *Nat. Photonics* **12**, 578–589 (2018).
2. Zheng, G. *et al.* Wide-field, high-resolution Fourier ptychographic microscopy. *Nat. Photonics* **7**, 739–745 (2013).
3. Bon, P. *et al.* Quadriwave lateral shearing interferometry for quantitative phase microscopy of living cells. *Opt. Express* **17**, 13080 (2009).
4. Wang, Z. *et al.* Spatial light interference microscopy (SLIM). *Opt. Express* **19**, 1016 (2011).
5. Tian, L. *et al.* Quantitative differential phase contrast imaging in an LED array microscope. *Opt. Express* **23**, 11394 (2015).
6. Popescu, G. *et al.* Optical imaging of cell mass and growth dynamics. *Am. J. Physiol. - Cell Physiol.* **295**, 538–544 (2008).
7. Wang, R. *et al.* Dispersion-relation phase spectroscopy of intracellular transport. *Opt. Express* **19**, 20571 (2011).
8. Taylor, R. W. *et al.* Interferometric Scattering (iSCAT) Microscopy and Related Techniques. *Label-Free Super-Resolution Microscopy* (ed. Astratov, V.) 25-65 (2019).
9. Young, G. *et al.* Interferometric Scattering Microscopy. *Annu. Rev. Phys. Chem.* **70**, 301–322 (2019).
10. Holanová, K. *et al.* Optical imaging and localization of prospective scattering labels smaller than a single protein. *Opt. Laser Technol.* **109**, 323–327 (2019).

11. Young, G. *et al.* Quantitative mass imaging of single biological macromolecules. *Science* **360**, 423–427 (2018).
12. Park, J. *et al.* Long-term cargo tracking reveals intricate trafficking through active cytoskeletal networks in the crowded cellular environment. *Nat. Commun.* **14**, 1–11 (2023).
13. Küppers, M. *et al.* Confocal interferometric scattering microscopy reveals 3D nanoscopic structure and dynamics in live cells. *Nat. Commun.* **14**, 1–12 (2023).
14. Biswas, A. *et al.* Mapping Cell Membrane Fluctuations Reveals Their Active Regulation and Transient Heterogeneities. *Biophys. J.* **113**, 1768–1781 (2017).
15. Shaked, N. T. *et al.* Off-axis digital holographic multiplexing for rapid wavefront acquisition and processing. *Adv. Opt. Photonics* **12**, 556 (2020).
16. Ishigane, G. *et al.* Label-free mid-infrared photothermal live-cell imaging beyond video rate. *Light Sci. Appl.* **12**, (2023).
17. Kashkanova, A. D. *et al.* Precision size and refractive index analysis of weakly scattering nanoparticles in polydispersions. *Nat. Methods* **19**, 586–593 (2022).
18. Walther, Tobias C *et al.* Lipid Droplets And Cellular Lipid Metabolism. *Annu Rev Biochem* **81**, 687–714 (2012).
19. Hugonnet, H. *et al.* Improving Specificity and Axial Spatial Resolution of Refractive Index Imaging by Exploiting Uncorrelated Subcellular Dynamics. *ACS Photonics* **11**, 257–266 (2024).
20. Umeda, K. *et al.* Activity-dependent glassy cell mechanics II: Nonthermal fluctuations under metabolic activity. *Biophys. J.* 1–36 (2023).
21. Green, D. R. *et al.* Cell death signaling. *Cold Spring Harb. Perspect. Biol.* **7**, a006080 (2015).
22. Zamaraeva, M. V. *et al.* Cells die with increased cytosolic ATP during apoptosis: A bioluminescence study with intracellular luciferase. *Cell Death Differ.* **12**, 1390–1397 (2005).
23. Horio, T. *et al.* Visualization of the dynamic instability of individual microtubules by dark-field microscopy. *Nature* **321**, 605–607 (1986).
24. Cheng, C. Y. *et al.* High-speed imaging and tracking of very small single nanoparticles by contrast enhanced microscopy. *Nanoscale* **11**, 568–577 (2019).
25. Toda, K. *et al.* Adaptive dynamic range shift (ADRIFT) quantitative phase imaging. *Light Sci. Appl.* **10**, 1–10 (2021).
26. Olsén, E. *et al.* Dual-Angle Interferometric Scattering Microscopy for Optical Multiparametric Particle Characterization. *Nano Lett.* **24**, 1874–1881 (2024).
27. Zhou, N. *et al.* Quasi-Isotropic High-Resolution Fourier Ptychographic Diffraction Tomography with Opposite Illuminations. *ACS Photonics* **10**, 2461–2466 (2023).
28. Bellisola, G. *et al.* Infrared spectroscopy and microscopy in cancer research and diagnosis. *Am. J. Cancer Res.* **2**, 1–21 (2012).
29. Cheng, J. X. *et al.* Vibrational spectroscopic imaging of living systems: An emerging platform for biology and medicine. *Science.* **350**, aaa8870 (2015).
30. Tkach, M. *et al.* Communication by Extracellular Vesicles: Where We Are and Where We Need to Go. *Cell* **164**, 1226–1232 (2016).
31. Nishizawa, K. *et al.* Feedback-tracking microrheology in living cells. *Sci. Adv.* **3**, 1–12 (2017).

Methods

BiQSM system

A detailed schematic of the BiQSM system is provided in Supplementary Note 1. Figure S1 illustrates the visible light source, which is based on the second harmonic generation (SHG) of a homemade femtosecond ytterbium-doped fiber mode-locked laser at a repetition rate of 63 MHz. After amplification using a ytterbium-doped fiber amplifier (YDFA) and compression with a grating pair (T-1000-1040-12.3x12.3-94, LightSmyth Technologies), the pulses are focused onto a Periodically Poled Stoichiometric Lithium Tantalite (PPSLT) crystal (Fan-out PPMgSLT, OXIDE). This setup generates a visible light source at 515 nm with an average power of approximately 100 mW. The spectral bandwidth is 2 nm, determined by the phase-matching condition. The resulting coherence length of $\sim 709 \mu\text{m}$ effectively suppresses interference between scattered light and undesired reflections from optical components, such as internal reflections from the objective lens.

Figure S2 illustrates the BiQSM system, which employs a spatial-frequency multiplexing method for off-axis DH using Mach-Zehnder interferometers. The visible light is introduced into the Mach-Zehnder interferometers in FS and BS imaging systems through a single-mode fiber and a fiber beamsplitter. In the sample arm of the interferometer, the illumination angle is slightly tilted ($\text{NA} \sim 0.3$) only for BS, achieved through two wedge prisms (PS810-A). This tilt is designed to minimize the internal reflected light reaching the image sensor. For both the FS and BS systems, the sample image is magnified in the image sensor plane for holographic measurement (VLXT-17M.I, Baumer) by a factor of 208 using an objective lens (UPLAPO100XOHR, Olympus) and relay lenses. The reference lights are directed to the image sensor at distinct off-axis angles between the FS and BS systems, following adjustments to the optical path length, beam size, and polarization to match those of the sample light. The FOV and half-pitch resolution are $44 \mu\text{m}$ and 193 nm , respectively.

Temporal noise calculation

For temporal noise evaluation, we captured 500 frames of no-sample images at 500 fps and calculated frame-to-frame differential SA images for both FS and BS imaging. Subsequently, the temporal standard deviation (STD) of the resulting 499 differential images was calculated at each pixel, generating temporal STD maps. The mean value of $200 \text{ pixels} \times 200 \text{ pixels}$ in the temporal STD maps was evaluated as temporal SA noise, which is equivalent to the minimum detectable SA.

The theoretical temporal SA noise due to optical shot noise can be expressed as

$$\delta SA^{\text{shot}} = 2 \sqrt{\frac{(4-\pi)A_{\text{aperture}}}{2v^2 N_{\text{electron}} A_{\text{sensor}}}} \quad (\text{Eq. 2})$$

where N_{electron} represents the average number of electrons in the hologram contributing to SA image reconstruction,

A_{sensor} and A_{aperture} denote the total and cropped pixel areas in spatial frequency space, respectively, and v symbolizes the visibility. Eq. 2 is derived from the temporal phase noise in off-axis DH¹⁶, incorporating an additional factor of $\sqrt{(4 - \pi)/2}$. This factor arises from error propagation using Eq. 1 under the assumption that the amplitude noise follows the same Gaussian distribution as phase noise. N_{electron} is calculated from the image sensor's output using a full-well capacity of 100 ke⁻ and a bit depth of 12. Visibility is determined using the procedure described in our previous publication¹⁶. The values of A_{sensor} and A_{aperture} are 1,048,576 (1024×1024 pixels) and 41,548 ($\pi/4 \times 230 \times 230$ pixels), respectively. By substituting these parameters into Eq. 2, the theoretical temporal noise map is calculated.

Preparation of samples

The polystyrene beads (151 ± 3 nm, ThermoFisher, 3150A) and silica beads (203 ± 12 nm and 52 ± 3 nm, nanoComposix, SISN200-25M and SISN50-25M) were suspended in water within a glass bottom dish for the experiment presented in Fig. 2.

COS7 cells were cultured on a glass bottom dish with high-glucose Dulbecco's modified eagle medium (DMEM), which contains L-glutamine, phenol red, and HEPES (FUJIFILM Wako). The medium was supplemented with 10% fetal bovine serum (Cosmo Bio) and 1% penicillin-streptomycin-L-glutamine solution (FUJIFILM Wako) at 37°C in a 5% CO₂ atmosphere. In the experiment represented in Fig. 4, time-lapse imaging was conducted at 5-minute intervals, starting 10 minutes after transferring the sample from the incubator to the measurement setup. The experiment was performed at room temperature (23.5 °C) under CO₂-depleted conditions.

Beads measurement

In the experiment shown in Fig. 2, a series of holograms was recorded at 500 fps. The E_{bg} images were generated by averaging 200 images in which no beads were present. Specifically, a window of 401 frames was selected—spanning from 200 frames before to 200 frames after the beads image shown in Fig. 2. Within this window, the first 100 frames (i.e. frames -200 to -101 relative to the beads image) and the last 100 frames (i.e. frames +101 to +200) were averaged separately. The two resulting averages were then combined to form the final background image.

The FS and BS cross-sections $\sigma_{\text{FS(BS)}}$ were determined by spatially integrating the SA images using the following equation:

$$\sigma_{\text{FS(BS)}} = \iint |SA_{\text{FS(BS)}}|^2 dx dy.$$

Prior to integration, numerical focusing was performed on the beads in the SA images, followed by Gaussian fitting to suppress background noise.

Dynamic image calculation

The dynamic images were calculated according to the procedure described below. A corresponding figure illustrating this process is presented in Supplementary Note 3. To suppress spatially uniform frame-by-frame temporal variations caused by laser intensity noise and optical path length difference variation between the sample and reference arms, each amplitude and phase image was normalized by the spatial average of the corresponding frame. Additionally, long-term variations exist in the spatial distribution of the background image (E_{bg}), primarily resulting from air fluctuations and sample stage drift. These variations exhibit a spatially low-frequency global pattern, as shown in Fig. S4a, where neighboring pixels display nearly identical background fluctuations. To compensate for these long-term variations, the value of each pixel was corrected by subtracting the mean value calculated from its neighboring 11×11 pixels (Fig. S4b), effectively removing spatially global background fluctuations. Then, a numerical band-pass filter was applied to the temporal evolution data of each pixel. Finally, the temporal standard deviation of each pixel was calculated to generate the 2D dynamic image map.

Data availability

The data provided in the manuscript is available from the corresponding author upon reasonable request.

Acknowledgments

This work was financially supported by Japan Society for the Promotion of Science (23H00273), JST FOREST Program (JPMJFR236C), Precise Measurement Technology Promotion Foundation, and UTEC-UTokyo FSI Research Grant.

Author contributions

K.T. conceived the concept of the work. K.T. and K.H. designed and developed the BiQSM system. T.N. and K.H. constructed the visible light source. K.H. performed the experiments and analyzed the experimental data. K.H., K.T., and T.I. discussed the interpretation of the results. T.I. supervised the work. K.H., K.T., and T.I. wrote the manuscript with inputs from the other authors.

Competing interests

K.H, K.T. and T.I. are inventors of patents related to the BiQSM system.

Supplementary information for Bidirectional quantitative scattering microscopy

Kohki Horie¹⁺, Keiichiro Toda²⁺, Takuma Nakamura² and Takuro Ideguchi^{1,2,*}

¹ Department of Physics, The University of Tokyo, Tokyo, Japan

² Institute for Photon Science and Technology, The University of Tokyo, Tokyo, Japan

⁺These authors contributed equally to this work

* Corresponding author: ideguchi@ipst.s.u-tokyo.ac.jp

Supplementary Note 1: Detailed schematic of BiQSM.

Figures S1 and S2 represent a detailed schematic of a visible light source and microscopy setup in BiQSM system, respectively.

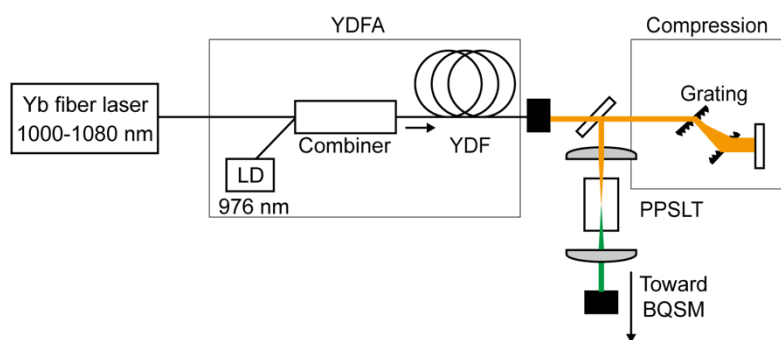


Fig. S1 Schematic of a visible light source in BiQSM system. Yb fiber: Ytterbium-doped fiber. YDFA: Ytterbium-doped fiber amplifier. LD: laser diode. PPSLT: Periodically poled stoichiometric lithium Tantalite.

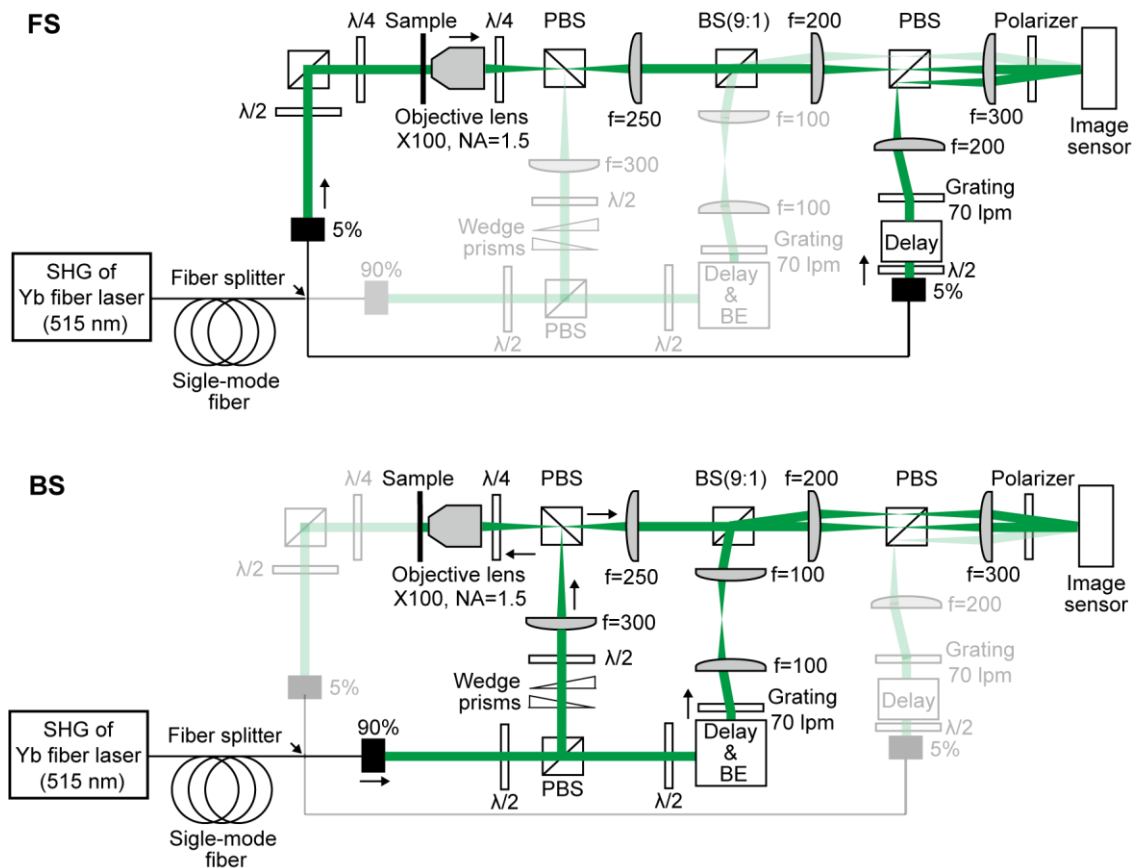


Fig. S2 Schematic of BiQSM system. FS (top) and BS (bottom) imaging system. SHG: second harmonic generation. $\lambda/4$ and $\lambda/2$: quarter- and half-wave plate. PBS: polarizing beamsplitter. BE: beam expander.

Supplementary Note 2: FS-BS correlation analysis for determining refractive index and size of small particles.

Figure S3a plots the measured values of the FS/BS cross-section ratio against the FS cross-section for silica beads (orange dots), alongside theoretical values for spherical objects of representative sizes and RIs (green dashed and solid reddish curves). For theoretical calculations, scattering cross-sections were obtained by integrating the Poynting vector derived from the analytical solution of the Mie-scattered electric field from spherical objects along the lateral axes at a specific axial position. To mitigate systematic errors in measured cross-sections caused by optical system imperfections, the measured cross-sections of silica beads were normalized by the mean measured cross-section of polystyrene beads (blue dots). Correspondingly, theoretical curves were also normalized by the cross-section of a polystyrene bead with a manufacturer-specified RI of 1.59 and a diameter of 151 nm. Figure S3b presents a mapping of RIs and sizes derived from measured cross-sections of silica beads. The RI and size of the silica beads were evaluated as 1.426 ± 0.006 and 206 ± 18 nm, respectively, closely aligning with the manufacturer's specifications of 1.43 and 203 ± 12 nm.

Two primary factors likely influence the precision of the particle characterization described above. The manufacturer-specified size variation of the beads (± 12 nm) is a primary determinant of the measurement precision (± 18 nm). However, an additional contributing factor must be considered, as the BS variation observed for polystyrene beads

is significantly larger than that for silica beads, as shown in Fig. 2c, despite the lower size variation specified for polystyrene beads (± 3 nm). In Fig. 2c, while the FS variations for both silica and polystyrene beads are comparable to the measurement SA noise inherent in FS imaging, the BS variation shows a strong dependence on the BS signal intensity. A possible contributor to this BS variation is a systematic error introduced during cross-section calculations. Specifically, numerical focusing of beads is conducted to facilitate robust Gaussian fitting; however, slight misfocusing can lead to deviations from the ideal Gaussian profile, causing fitting errors that may scale approximately in proportion to the BS signal intensity.

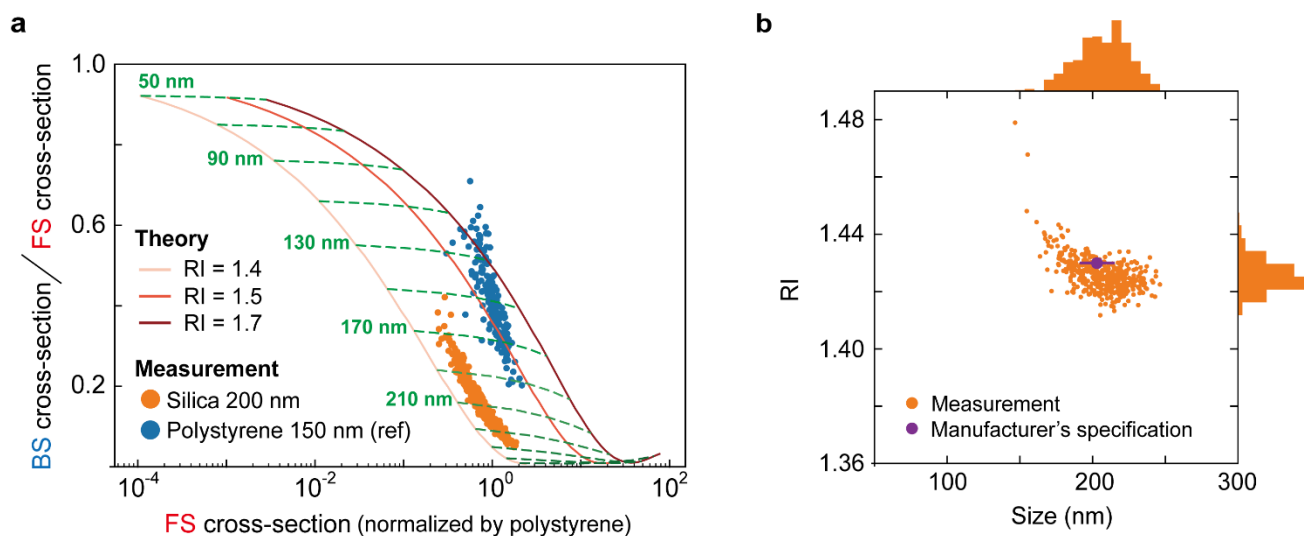


Fig. S3 FS-BS correlation analysis of beads for determining RI and size. **a** FS/BS cross-section ratio plotted against FS cross-section for silica beads. Orange dots represent measured values for silica beads (203 ± 12 nm, 412 particles), whereas the green dashed curves and solid reddish curves show theoretical predictions for spherical objects of varying sizes and RIs in an aqueous environment. The FS cross-section values are normalized by the mean measured cross-section for polystyrene beads (151 ± 3 nm, 204 particles, represented as blue dots). **b** RI and size mapping derived from the measured cross-sections of silica beads. The purple bar represents the manufacturer-specified size variation of the beads (± 12 nm).

Supplementary Note 3: Calculation procedure for dynamic images.

Figure S4a represents the temporal differential image obtained by comparing SA images at $t = 0$ s and $t = 10$ s. This differential image reveals a global change in E_{bg} as well as localized differential signals attributed to the movements of intracellular structures. Figure S4b illustrates the procedure used to calculate the dynamic SA image for each imaging pixel.

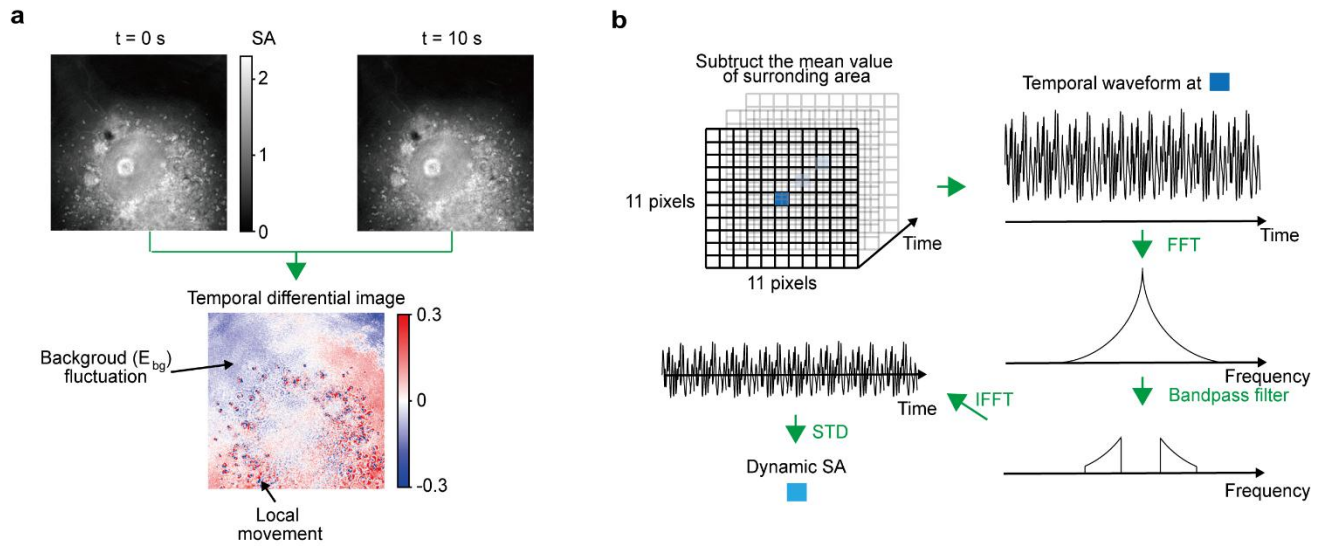


Fig. S4 Long-term temporal variations in background images and procedure for dynamic SA calculation. a SA images at $t = 0$ s and $t = 10$ s, and their differential image. **b** Procedure for calculating dynamic SA for each image pixel. FFT: Fast Fourier transform. IFFT: inverse fast Fourier transform. STD: standard deviation.